points are represented by the data symbols superimposed on the correlation. None of the free-flight data contained in Fig. 1 were used in the original correlation. These data are for a different nosetip material and a different range of nosetip radii than were considered in the correlation. The correlation appears to be useful even though a nosetip material other than that of the data base is being considered. The correlation represents the alternate material in that the data generally fall into the regimes indicated by the correlation. The scaling with nosetip radius, however, appears to result in an underprediction of nosetip normal force as the flight 9 result of Fig. 1 indicates. The present study considers large radii nosetips and thus the values of nosetip normal force determined may be smaller than would be expected. Further comparisons indicate a need for continuing work in extending this type of correlation to the general case.

All of the information compiled thus far is then used as input for a six-degree-of-freedom, modular, trajectory simulator. Variations in the aerodynamic, material, metrological, and launch conditions may then be investigated using sensitivity techniques. The trajectory simulator and the previously mentioned analytic techniques have been used to simulate conditions for which flight test data is available. Within the limitations of the technique, excellent agreement has been noted between simulated parameters and parameters determined from the flight test data. Such agreement provides further confidence in the methodology.

In order to assess the effects of nosetip shape change upon dispersion, surface roughness heights of two-tenths, four-tenths, and six-tenths of a mil were used to influence the boundary-layer transition criterion in the nosetip shape-change code, thus generating different nosetip shape-change histories. The use of a surface roughness parameter to influence shape change has been investigated and found useful.[4]

Typical impact shapes generated for a range of surface roughness parameter values are given in Fig. 2. Numerous trajectory simulations were made using the generated nosetip shape histories. Representative results of this study are shown in Fig. 3, where impact variation distance for a blunted sphere cone ($R_n/R_B > 0.2$), relative to a nominal, nonablating, seven-percent static-margin sphere-cone trajectory, is plotted vs static margin. Small lift-generated variations occur with static margin for any nosetip history.

The very significant result of this analysis is indicated by the impact variations on the order of 250 ft over the small nosetip shape uncertainty regime indicated for each static margin. From this plot it is concluded that nosetip shape changes significantly affect re-entry vehicle flight performance and can lead to significant impact coordinate variations. The variations presented are due to both lift and drag. Analysis at the seven-percent static margin point shows drag contributing 65% of the impact variation while lift contributes 35%. The variation of surface roughness, shape-generated, impact variation factor is not monotonic because ablative nosetip drag effects may either increase or decrease the blast wave statement (downstream) determined value at various points over the re-entry trajectory. Nosetip shape-change effects are still being analyzed and improvements are being made to simulation techniques.

References

[1] "User's Manual Steady-State Analysis of Ablating Nose Tips—SAANT," UM-73-38, Aerotherm Div., Acurex corp., Mountain View, Calif., Sept. 1973.

[2] Chernyi, G. C., *Introduction to Hypersonic Flow*, Academic Press, New York and London, 1961, pp. 201-234.

[3] Crenshaw, P. J., "Asymmetric Nosetip Transition Effects on Re-Entry Vehicle Trim, Nosetip Shape and Aerodynamics," submitted for publication in *Journal of Spacecraft and Rockets*, 1975.

[4] Welsh, W. E. Jr., "Shape and Surface Roughness Effects on Nosetip Ablation," *AIAA Journal*, Vol. 8, Nov. 1970, pp. 1983-1989.

Evaluation of Boron/Aluminum Tubes in Compression

A. C. Knoell*
Jet Propulsion Laboratory, Pasadena, Calif.

Introduction

CONSIDERABLE attention has recently been given to the development and application of boron/aluminum k/Al) composite material to aircraft[1,2] and spacecraft[3-5] structures. The results of these investigations and others have shown that B/Al offers the potential of improved structural performance at reduced weight when compared to conventional metal counterpart structures. Furthermore, these investigations have also indicated that such improved performance can be confidently and economically gained as a result of improved fabrication techniques and more widespread usage of the material.

Using these results, a brief analytical and experimental investigation was performed to determine the compressive behavior of B/Al tubes. The investigation consisted of determining the full scale column and local crippling strengths of six B/Al tubes. The purpose of the investigation was to gain hardware experience in a limited evaluation of the material for application to spacecraft truss structures. It was recognized that the results of this investigation could also be coupled with other available analytical and experimental data on B/Al, thereby contributing at least in a small manner to an expanded data base of the material. This Note presents the results of that investigation.

Specimen Description

All tubes used in the investigation were fabricated of unidirectional B/Al aligned parallel to the long axis of the tubes with integrally diffusion-bonded titanium end collars. The fiber volume fraction ranged from 47 to 50%. Fiber bend tests performed on leached-out filaments of the material indicated a fiber strength in excess of 500,000 psi.

After fabrication, all tubes were ultrasonically inspected by a through transmission technique. All tubes gave excellent indications of tube/collar bonding. The tubes were also inspected for physical defects; none were observed except for minor localized overetching of one specimen.

The tubes consisted of 3- and 4-ply laminates and were nominally 1.70 in. in diameter by 36 in. long. The specific physical characteristics of the tubes are summarized in Table 1.

Experimental Procedure

All tubes were tested in static compression at a loading rate of approximately 1800 lbf/min at room temperature under ambient conditions. Male end-fitting attachments were used to stabilize the column against lateral motion. A continuous recording of load vs displacement was made for all test specimens. In the case of specimen S/N-1, which was in-

Submitted May 7, 1975; presented as Paper 75-789 at the AIAA/ASME/SAE 16th Structures, Structural Dynamics, and Materials Conference, Denver, Colorado, May 27-29, 1975; revision received June 12, 1975. This work was supported under NASA Contract NAS 7-100. Organizations that contributed were NASA-JSC, Rockwell International Space Division, and General Dynamics Convair Division; W. Jensen and B. Montgomery of JPL conducted the experiments and E. Robinson, formerly of JPL, developed the early arrangements for the program.

Index categories: Materials, Properties of; Structural Composite Materials (including Coatings); Structural Stability Analysis.

*Member of Technical Staff. Associate Fellow AIAA.

Table 1 Tube characteristics

S/N	Plies	Wall thickness (in.)	i.d. (in.)	Length (in.)	Wt (lb)
1	3	0.021	1.703	36.12	0.50
3	3	0.021	1.704	36.11	0.50
5	3	0.021	1.700	36.18	0.52
7	3	0.020	1.703	36.09	0.51
6	4	0.027	1.688	36.12	0.66
8	4	0.026	1.689	36.11	0.65

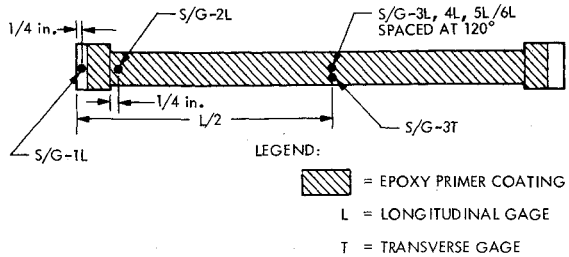

Fig. 1 S/N-1 test instrumentation location.

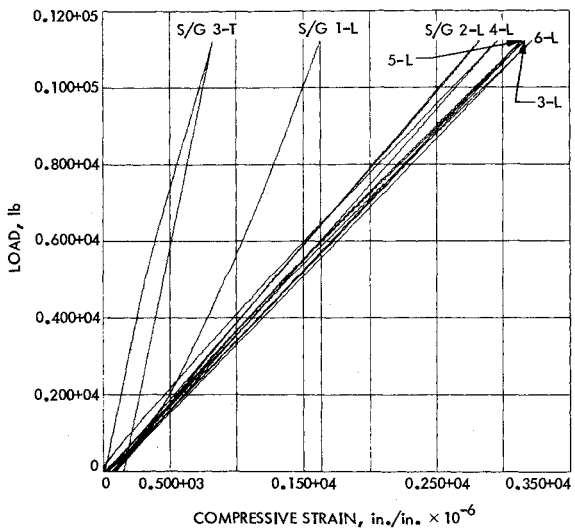

Fig. 2 Load-strain response for specimen S/N-1.

Table 2 Full-scale column tests

S/N	Plies	Test mode[a]	Failure load (lb)	Comments
1	3	A	11,200	Failed at tube-fitting interface
3	3	A	12,900	Failed at tube-fitting interface
5	3	A	14,400	Failed at tube-fitting interface
7	3	B	13,600	Failed at tube-fitting interface
6	4	B	17,500	Failed at tube-fitting interface; visible bowing of tube prior to failure
8	4	B	14,000	Failed at tube-fitting interface; visible bowing of tube prior to failure

[a] Test modes: A = Direct platen compression on Ti end fittings. No secondary fittings to simulate pin-ended condition. B = Secondary fitting used to simulate pin-ended condition.

Table 3 Short column results

S/N	Plies	Failure load (lb)	Predicted failure load (lb)	Comments
5A	3	13,000	15,000	Failed in tube near fitting
7A	3	15,100	15,000	Failed in tube near fitting
6A	4	20,300	27,300	Failed in tube near fitting

strumented as described below, continuous digital recording was made of load vs strain for each gage.

Seven unidirectional strain gages were installed on specimen S/N-1 as shown in Fig. 1. The instrumentation was arranged to assess column loading eccentricity and determine modulus of elasticity, Poisson's ratio, load transfer in the vicinity of the collar and linearity of response to failure. Gages 1L, 2L, and 3L were collinear with gage 3T mounted adjacent to gage 3L. Gages 3L, 4L, 5L, and 6L were located to monitor eccentric loading effects. The epoxy primer in the immediate vicinity of gages 2L through 6L was removed prior to gage installation.

Results

The elastic properties and load transfer capability of the collar were determined by application of three cycles of static load on tube S/N-1 to 50% of design ultimate load. Linearity of response was also demonstrated as indicated by the load vs strain data (Fig. 2) taken to failure. These data were obtained after shimming and low-level loading of the column to bring the readings of gages 3L through 6L within 10% of their average strain value. From these data it was determined that E_L (elastic modulus) = 31.5 $\times 10^6$ psi and ν_{LT} (major Poisson's ratio) = 0.26. These values and others obtained from the literature were then used in design analyses of the tubes. After testing specimen S/N-1 for elastic behavior, this specimen and all remaining tubes were statically loaded to failure. The results of these tests are summarized in Table 2.

Since all tubes failed near a collar end-fitting, short (12-in.) column specimens were taken from unfailed and undamaged sections of tubes 5, 7, and 6 for further testing. These tubes were set in epoxy in aluminum female end-fittings and similarly tested to failure. The results of these tests are given in Table 3.

The short column tests were run to determine the local buckling strength of such tube constructions. The objective here was to obtain experimental data for comparison with analytical prediction methods. Local crippling strengths were computed using classical (wave pattern buckle) and large deflection (diamond shape buckle) theories. It was found that computations using the large deflection theory as developed by Kuenzi[6] yielded the best agreement with experimental data. The predicted values without application of empirical knockdown factors are given in Table 3. A comparison of the data for long and short columns suggests that local buckling may have occurred during full-scale testing of the 3-ply tubes.

Conclusions

The tubes were designed as beam column members to fail under combined stress at an ultimate load of 10,000 lb. The results of the full-scale column tests (Table 2) show that the design objective was met with a minimum margin of 12% on the design ultimate load. A stability failure mode was not clearly evident in the full-scale tests.

The results given in Table 2 are also consistent with other B/Al tube data reported in the literature,[5] thereby contributing to improved confidence in its application to spacecraft truss structures. As indicated in Fig. 2, the tubes

demonstrated an ideal linear behavior to failure with reasonably repeatable performance.

The short column analysis and experimental tube data given in Table 3 indicate that a suitable analytical procedure exists for predicting the local instability of B/Al columns. It is important to note that such a capability, coupled with the generally more accurate prediction techniques relative to column buckling and strength, greatly enhances the capability to design and analyze B/Al tubular structures. The limited data suggest that an empirical knockdown factor of approximately 0.75 be applied to predictions using the analysis procedure to improve correlation between theoretical and test data. More correlation studies are required to demonstrate general application of the procedure over a wider range of specimen diameter to thickness (D/t) ratios.

References

[1]Miller, M. F., Schaeffer, W. H., and Weisinger, M. D., "Development of Improved Metal-Matrix Manufacturing Techniques for Aircraft Structures," AFML-TR-71-181, Aug. 1971, Air Force Materials Lab, Wright Patterson Air Force Base, Ohio.

[2]Wennhold, W. F., "Design and Fabrication of a B/Al Composite Wingbox Test Specimen," GD Report CASD-NSC73-005, July 1973.

[3]Brown, E. P. and Hepper, R. H., "Boron-Aluminum Structural Component for Shuttle," *SAMPE Quarterly*, Vol. 3, July 1972, pp. 12-16.

[4]Robertson, A. R. and Miller, M. F., "Boron/Aluminum for Space Applications," *National SAMPE Technical Conference Series*, Vol. 6, Oct. 1974, pp. 361-368.

[5]Weisinger, M. D., Forest, J. D., and Miller, M., "Feasibility Demonstration Program for the Application of Boron/Aluminum to Space Shuttle," GD Report CASD-NAS-74-017, May 1974.

[6]Kuenzi, E., "Buckling of Layered Orthotropic and Sandwich Cylindrical Shells in Axial Compression," TND 1510, Dec. 1962, NASA.

Effect of Nonsymmetric Damping on Trim Magnification of Rolling Re-entry Vehicles

Charles W. Ingram*
Systems Research Laboratories, Inc., Dayton, Ohio

and

Frank M. Sawyer†
Air Force Flight Dynamics Laboratory, Wright-Patterson Air Force Base, Ohio

Nomenclature

A = $\pi d^2/4$, reference area, ft^2
C_m = pitching moment coefficient, M_y/QAd
C_{m_σ} = $(\partial C_m/\partial\sigma)_{\sigma-0}$ in-plane static stability derivative 1/rad
$C_{m_q}+C_{m_\alpha}$ = $\partial C_m/\partial(qd/V)+\partial C_m(\alpha d/V)$, in-plane damping derivative, 1/rad
$C_{n_r}-\cos\alpha \times C_{n_\beta}$ = $\partial C_n/\partial(rd/V)-\cos\alpha\ \partial C_n/\partial(\beta d/V)$, out-of-plane damping derivative, 1/rad
C_{m_ϵ} = $C_{m_\sigma}\delta_{t_0}$, aerodynamic asymmetry coefficient
d = model base diameter, ft
I = transverse moment of inertia, slug-ft^2
I_x = axial moment of inertia, slug-ft^2
M_x, M_y, M_z = moments about aerodynamic axes, ft-lb
Q = dynamic pressure, lb/ft^2
V = velocity fps
$p.q.r$ = roll, pitch, and yaw rates, respectively, rad/sec
X, Y, Z = inertial axes (see Fig. 1)
x, y, z = aerodynamic axes (see Fig. 1)
δ_{t_0} = nonrolling trim angle, rad or deg
σ = resultant angle of atack, rad or deg
$\dot\phi$ = coning rate, (see Fig. 1) rad/sec
$\dot\psi$ = body roll rate, (see Fig. 1) rad/sec

Received May 21, 1975.
Index category: Entry Vehicle Dynamics and Control.
*Senior Scientist, Aerosystems Research Division. Member AIAA.
†Aerospace Engineer, Controls Criteria Branch.

Introduction

THE symmetric assumption of the linear aeroballistic theory[1] requiring equality between the in-plane and out-of-plane aerodynamic derivatives, i.e.,

$$C_{m_q}+C_{m_{\dot\alpha}}=C_{n_r}-\cos\alpha\ C_{n_{\dot\beta}} \tag{1}$$

has been shown to be theoretically[2,3] and experimentally[4-6] invalid when the restoring moment C_m is nonlinear with angle of attack. In present wind tunnel tests the nonlinearity of C_m and $C_{m_q}+C_{m_{\dot\alpha}}$ with angle of attack are usually determined while the inequalities of in-plane and out-of-plane damping derivatives are neglected. The same is true for computer stability and performance analyses. It is the purpose of this Note to demonstrate the effects of nonsymmetric damping derivatives on the resultant angle of attack of a re-entry vehicle with slight aerodynamic asymmetries passing through resonance.

Computer Investigations

The aerodynamic axis system[7] is shown in Fig. 1. The moment equations, for a constrained center of gravity, are

$$I_x\dot p=M_x$$

$$I\ddot\sigma+I_xp\dot\phi\ \sin\sigma-I\dot\phi^2\sin\sigma\ \cos\sigma=M_y$$

$$I\dot\phi\ \sin\sigma+2I\dot\sigma\dot\phi\ \cos\sigma-Ixp\sigma=M_z$$

where

M_x = Constant roll moment

$$M_y=\left\{C_m+(\sigma d/V)\ (C_{m_q}+C_{m_{\dot\alpha}})+C_{m_\epsilon}\cos\psi\right\}QAD$$

$$M_z=\left\{(\phi d/V)\sin\phi(C_{n_r}-\cos\alpha C_{n_{\dot\beta}})+C_{m_\epsilon}\sin\psi\right\}QAd$$

$$\psi=p-\phi\ \cos\sigma$$

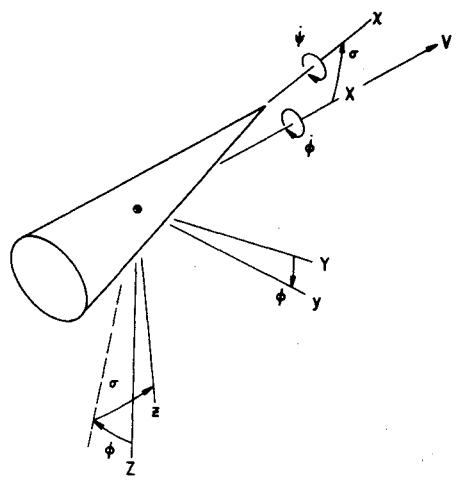

Fig. 1 Aerodynamic axes system.